

# Optically heralded microwave photon addition

---

In the format provided by the  
authors and unedited

# Supplementary information: Optically heralded microwave photon addition

Wentao Jiang,<sup>\*</sup> Felix M. Mayor,<sup>\*</sup> Sultan Malik, Raphaël Van Laer,<sup>†</sup> Timothy P. McKenna, Rishi N. Patel, Jeremy D. Witmer, and Amir H. Safavi-Naeini<sup>‡</sup>

*Department of Applied Physics and Ginzton Laboratory,  
Stanford University, 348 Via Pueblo Mall, Stanford, California 94305, USA*

(Dated: May 15, 2023)

## Supplementary Note 1. DEVICE DESIGN

The optomechanical design is similar to previous piezo-optomechanical transducer works [1, 2]. We design two different types of mirror unit cells, one optimized with both optical and mechanical bandgaps around the frequency of the localized modes for the optical and mechanical polarizations of interest, and one with only the optical bandgap while still allowing the mechanical mode to propagate. We first optimize the optomechanical crystal with a fully symmetric design using the first type of unitcell on both ends of the OMC, and optimize the defect cell geometries to maximize the product of the radiation-limited optical quality factor and the optomechanical coupling rate  $g_o$ . A cubic transition between the defect unit cell and the mirror unit cell forms the smooth confinement of the optical and mechanical mode. Unit cells on one side of the OMC are then replaced to be the second type, enabling the hybridization between the mechanical mode in the OMC and the hybrid Si-LN piezoelectric mode.

It is important to maximize the hybridization between the OMC mechanical mode and the Si-LN piezoelectric mode, so that the device is tolerant to fabrication variations. We note that the leaky mechanical mode from the OMC is mostly longitudinal, while the strong piezoelectric mode in the Si-LN structure is mostly in horizontal shear (SH) polarization. We use a  $45^\circ$  rotation between the OMC and the Si-LN structure to align the polarization between the longitudinal mode and SH mode, and achieve a hybridization with coupling strength  $J/2\pi \approx 42$  MHz. Similar to Ref. [3], we adopt *X*-cut thin-film LN to utilize the strong piezoelectricity of the SH mode, where its largest piezoelectric component  $d_{24} \approx 70$  pm V<sup>-1</sup> couples *YZ* shear to electric field along the crystal *Y* axis. The aluminum electrodes are patterned to be parallel to the crystal *Z* axis so that the electric field between them are parallel to *Y*. To prevent the mechanical mode from leaking into the substrate, we implement extra one dimensional phononic shields (1DPS) with a full bandgap around the mechanical frequency. The 1DPS is optimized separately for anchoring the Si-LN piezoelectric structure to take into account the aluminum electrodes.

## Supplementary Note 2. DEVICE FABRICATION

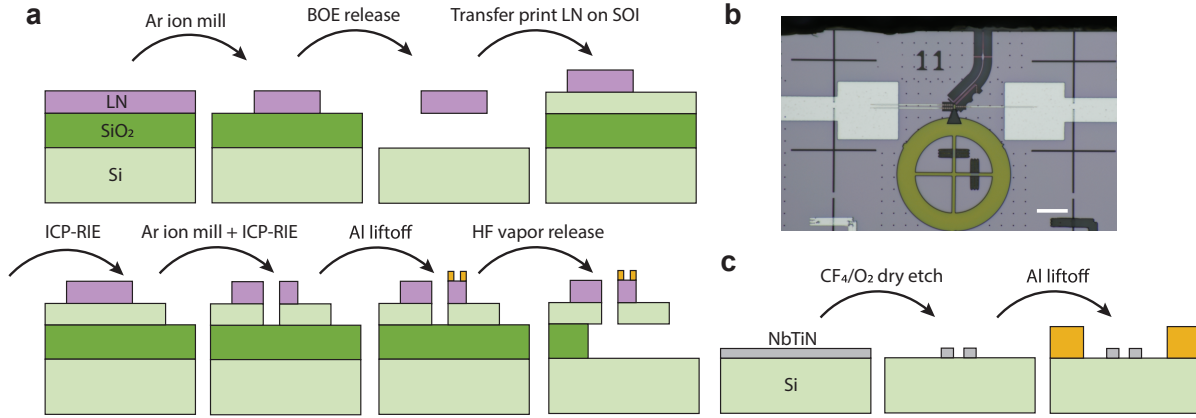
Patterning of thin film LN has been done with a wide variety of underlying substrates such as silicon, silica and sapphire. However, physical etching of LN is not directly compatible with the LN-on-SOI platform since the etch damages the surface of the silicon thin film and leads to significantly reduced optical quality factors. To avoid this issue, we pattern a thin film of LN on a separate LN-on-insulator sample and transfer print [4] it onto a pristine SOI chip. The fabrication process is summarized in Supplementary Figure 1. We start with 400 nm thick MgO-doped *X*-cut LN on a 3  $\mu$ m thick thermal silica buffer layer sitting on a 400  $\mu$ m thick silicon handle (commercially available from NanoLN). The LN film is first thinned to 290 nm with argon ion milling. The LN transducer and alignment marks are defined with electron beam lithography (EBL) using hydrogen silsesquioxane (HSQ) as the resist. The pattern is transferred to LN with a 265 nm deep etch using argon ion milling. The HSQ is stripped in buffered oxide etchant (BOE, 6:1) and the LN is then cleaned in dilute hydrofluoric acid (HF, 5 %). To etch the remaining LN slab and expose the silica, we carry out another 40 nm deep LN etch with blanket argon ion milling, followed by a clean in a piranha solution (3:1 98% sulfuric acid and 40% hydrogen peroxide). The LN is released by etching the silica in 6:1 BOE for 22 minutes which leads to a 3  $\mu$ m undercut of the thermal oxide. A piece of polydimethylsiloxane (PDMS) attached to a glass-slide which is mounted on a set of translational stages is lowered until it fully covers the LN sample. Due to its viscoelasticity [4], when rapidly lifting up the PDMS away from the sample, released LN

---

<sup>\*</sup> These authors contributed equally

<sup>†</sup> Present address: Department of Microtechnology and Nanoscience, Chalmers University of Technology, Sweden

<sup>‡</sup> safavi@stanford.edu



Supplementary Figure 1. **Device fabrication.** **a**, Fabrication process of the transducer chip. **b**, Optical image of the transducer device after the full fabrication process. The edge of the chip is diced to expose the on-chip optical coupler. **c**, Fabrication process of the microwave chip.

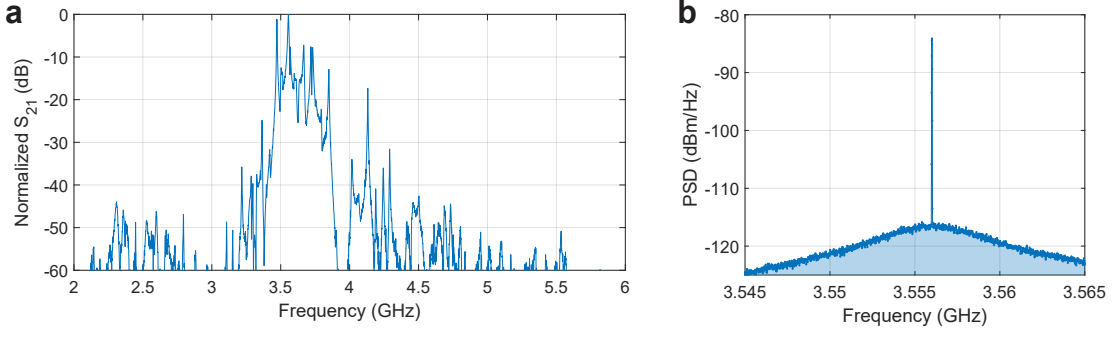
patterns break off from their anchors and stick to the PDMS. We then make the PDMS with LN touch down onto a SOI piece (220 nm thick silicon device layer, 3  $\mu\text{m}$  thick buried oxide, 725  $\mu\text{m}$  silicon handle) that has been cleaned in a piranha solution. By slowly peeling off the PDMS from the SOI substrate, the LN patterns are released from the PDMS and adhere to the silicon. We could simultaneously transfer print more than 100 devices, and typically achieve a  $> 95\%$  transfer print yield. Subsequently, the chip is annealed for 8 hours at 500  $^{\circ}\text{C}$  to improve the LN-Si adhesion. This is followed by a clean in piranha solution. The transfer print causes a  $\sim 0.1\%$  relative displacement between separated patterns. We attach alignment marks within 30  $\mu\text{m}$  of every device to enable sub-30 nm alignment error on EBL masks after the transfer print.

We pattern the silicon with aligned EBL and do an inductively coupled plasma (ICP) - reactive ion etch (RIE) using a  $\text{Cl}_2$  and  $\text{HBr}$  gas chemistry. The device is still attached to the transfer printed alignment mark which would cause mechanical loss. We therefore do another aligned EBL to pattern a small window where we argon ion mill the LN followed by ICP-RIE to etch through the silicon device layer. Subsequently, we expose the oxide in the areas of the chip that do not have any devices by etching the silicon device layer with ICP-RIE after having defined etch windows with photolithography. The sample is cleaned a final time in a piranha solution before metalization. The transducer electrodes are patterned with aligned EBL. We evaporate 55 nm aluminum at three different angles ( $-66^{\circ}, 0^{\circ}, 66^{\circ}$ ) to help the electrodes climb the LN from the silicon, and lift-off in N-Methyl-2-pyrrolidone (NMP) at 80  $^{\circ}\text{C}$ . The wirebond pads are defined with photolithography, and we evaporate 250 nm aluminum followed by lift-off in NMP at 80  $^{\circ}\text{C}$ . Finally, the chip is diced close to the edge coupler and the devices are released in HF vapor. To accommodate fabrication uncertainties, the optomechanical crystals and the separation of the piezoelectric resonator electrodes in different transducer devices are scaled by  $\pm 2\%$  and  $\pm 5\%$  respectively.

The microwave resonator is fabricated on a separate die from the transducer to simplify fabrication and potentially reduce optically induced quasiparticle generation [2] by vertically offsetting the resonator from the optical fiber. We start with a 10 nm thin layer of niobium titanium nitride (NbTiN) on high-resistivity silicon. We use EBL to define the meander in HSQ resist and etch the NbTiN using RIE with a  $\text{CF}_4$  and  $\text{O}_2$  gas chemistry. The HSQ is stripped in 6:1 BOE. Finally, a 250 nm thick aluminum ground plane is defined with photolithography followed by evaporation and liftoff.

### Supplementary Note 3. ROOM TEMPERATURE MECHANICS-TO-MICROWAVE EXTERNAL COUPLING MEASUREMENT

The fabricated transducers can be measured at room temperature before integrating with the microwave chip, especially for characterizing the mechanics-to-microwave external coupling and optical quality factor. This allows us to select the best performing transducer for packaging and cooldown. Similar to the method described in Ref. [5], a microwave probe (GGB Industries, Picoprobe model 40A-GSG) is brought in contact with the on-chip electrodes of the piezo-optomechanical transducer. A red-detuned laser is used to enable the microwave-to-optical conversion and readout the converted sideband photon (Supplementary Figure 2). The coherent microwave input signal is then



Supplementary Figure 2. **Room-temperature conversion measurement and calibration.** **a**, Normalized microwave-to-optical conversion S parameter. Multiple mechanical modes are visible due to the high signal-to-noise ratio of the measurement. Two mechanical modes are strongly hybridized with the OMC mechanical mode and show much higher conversion efficiency than other modes. **b**, Calibration of the mechanics-to-microwave external coupling. The thermal-mechanical noise power (shaded area) is used to calibrate the optomechanical readout of the intracavity phonon number.

fixed at the peak conversion frequency, on resonance with one of the mechanical modes, and gives rise to a coherent intracavity phonon population

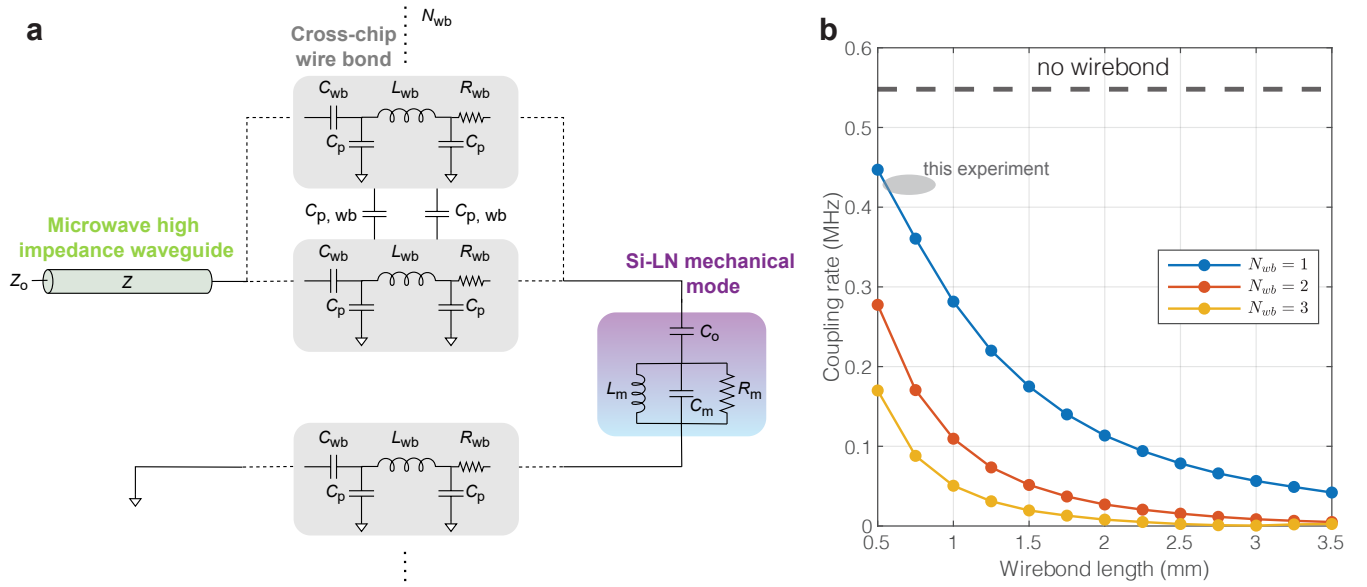
$$n_{\text{coh}} = \frac{4\gamma_{\mu}\dot{N}}{\gamma^2}, \quad (1)$$

where  $\gamma_{\mu}$  is the external coupling rate between the mechanical mode and the  $50\Omega$  microwave line,  $\gamma$  is the total mechanical linewidth, and  $\dot{N}$  is the input microwave photon flux. As shown in Supplementary Figure 2, both the coherent and the thermal phonons are converted to sideband photons, and measured on the microwave power spectrum from a fast photodetector output. To calculate the thermal phonon number and calibrate the optical readout, the device temperature is assumed to be 295 K. The coherent phonon number  $n_{\text{coh}}$  and the external coupling rate  $\gamma_{\mu}$  can then be calculated.

#### Supplementary Note 4. PIEZOELECTRIC COUPLING VIA CROSS-CHIP WIREBOND

The transducer and the microwave resonator are fabricated on separate chips and integrated together via cross-chip wirebonding. To understand the impact of wirebonds on the coupling rate between the two, we consider a lumped element circuit model of the wirebonds between the Si-LN mechanical mode of the transducer chip and the high-impedance waveguide mode of the microwave chip, as shown in Supplementary Figure 3. The Si-LN mechanical mode is modeled as a *RLC* circuit with parameters  $L_m = 195.6$  nH,  $C_m = 10.01$  fF,  $R_m = 45.4$  M $\Omega$ , and  $C_o = 0.11$  fF, estimated from a combination of finite-element simulation and room temperature piezo-optomechanical measurements. The microwave waveguide is modeled as a transmission line (FSR = 110 MHz,  $Z = 1000\Omega$ ). We model the signal and ground cross-chip wirebonds as series inductance  $L_{\text{wb}}$  with parasitic capacitance to the ground plane  $C_p$  in parallel, and a contact capacitance  $C_{\text{wb}}$  and a contact resistance  $R_{\text{wb}}$  in series. The wirebonds have mutual capacitance of  $C_{p,\text{wb}}$  between them. For a 25  $\mu\text{m}$  diameter wire, the inductance roughly scales as  $L_{\text{wb}} \sim 1$  nH/mm [6, 7]. The remaining wirebond parameters are estimated using finite-element electrostatic analysis with nominal values of  $C_p \sim 20$  fF,  $C_{\text{wb}} \sim 20$  pF,  $R_{\text{wb}} \sim 0.4\Omega$  [8], and  $C_{p,\text{wb}} \sim 12$  fF/mm. The model exhibits strong reduction in the coupling rate with increasing wirebond length and increasing number of wirebonds as seen in the plot in Supplementary Figure 3. This is due to the increase in parasitic capacitance of the wires to the ground plane and increase in mutual capacitance between the signal and ground wirebonds. Hence, to maximize the coupling rate, a single signal wirebond with length as short as possible is desirable.

We first considered placing the two chips next to each other with the optical edge coupler side of the transducer chip facing away from the microwave chip. However, the shortest possible wirebond in such a case is limited by the net distance between the terminals of the devices on the two chips which turns out to be significant. In this experiment, we utilize a different approach in which the two chips are wirebonded together with the optical edge coupler side of the transducer chip facing the microwave chip. To allow fiber access for optical coupling, the transducer is then flipped over and stacked vertically, resulting in a shorter wirebond with length on the order of 0.75 mm. Two small spacer chips are glued near the edge of the microwave chip with GE varnish to support the transducer chip. Not only



Supplementary Figure 3. **Cross-chip wire bond model.** **a**, Lumped element circuit model of the cross-chip wirebonds between the Si-LN mechanical mode of the transducer chip and the high-impedance waveguide mode of the microwave chip. The Si-LN mechanical mode is modeled as a  $RLC$  circuit (with parameters  $R_m$ ,  $L_m$ ,  $C_m$ , and  $C_o$ ) and the microwave waveguide is modeled as a transmission line (with a characteristic impedance of  $Z = 1000 \Omega$ ). The signal and ground cross-chip wirebonds are modeled as series inductance  $L_{wb}$  with parasitic capacitance to the ground plane  $C_p$  in parallel, a contact capacitance  $C_{wb}$  and a contact resistance  $R_{wb}$  in series. There are  $N_{wb}$  number of wirebonds with mutual capacitance  $C_{p,wb}$  between them. **b**, Coupling rate between the Si-LN mechanical mode and the microwave waveguide as a function of wirebond length for various values of  $N_{wb}$ . A shaded grey region shows the estimated coupling rate and the estimated wirebond length in this experiment.

does this approach give us a shorter wirebond, it also results in the microwave chip being in a different plane than the optical fiber which likely helps minimize optically induced quasiparticle generation.

- 
- [1] G. Peairs, M.-H. Chou, A. Bienfait, H.-S. Chang, C. Conner, É. Dumur, J. Grebel, R. Povey, E. Şahin, K. Satzinger, *et al.*, *Physical Review Applied* **14**, 061001 (2020).
  - [2] M. Mirhosseini, A. Sipahigil, M. Kalaei, and O. Painter, *Nature* **588**, 599 (2020).
  - [3] P. Arrangoiz-Arriola, E. A. Wollack, Z. Wang, M. Pechal, W. Jiang, T. P. McKenna, J. D. Witmer, R. Van Laer, and A. H. Safavi-Naeini, *Nature* **571**, 537 (2019).
  - [4] M. A. Meitl, Z.-T. Zhu, V. Kumar, K. J. Lee, X. Feng, Y. Y. Huang, I. Adesida, R. G. Nuzzo, and J. A. Rogers, *Nature Materials* **5**, 33 (2006).
  - [5] W. Jiang, R. N. Patel, F. M. Mayor, T. P. McKenna, P. Arrangoiz-Arriola, C. J. Sarabalis, J. D. Witmer, R. Van Laer, and A. H. Safavi-Naeini, *Optica* **6**, 845 (2019).
  - [6] J. Wenner, M. Neeley, R. C. Bialczak, M. Lenander, E. Lucero, A. D. O'connell, D. Sank, H. Wang, M. Weides, A. N. Cleland, and J. M. Martinis, *Supercond. Sci. Technol* **24**, 65001 (2011).
  - [7] S. Huang, B. Lienhard, G. Calusine, A. Vepsäläinen, J. Braumüller, D. K. Kim, A. J. Melville, B. M. Niedzielski, J. L. Yoder, B. Kannan, *et al.*, *PRX Quantum* **2**, 020306 (2021).
  - [8] Y. Zhong, H.-S. Chang, A. Bienfait, É. Dumur, M.-H. Chou, C. R. Conner, J. Grebel, R. G. Povey, H. Yan, D. I. Schuster, *et al.*, *Nature* **590**, 571 (2021).